LUND UNIVERSITY
Faculty of Science

A high-order harmonic pump-probe setup using annular-beam interferometers

Hampus Wikmark

Thesis submitted for the degree of Master of Science
Project duration: 9 months

Supervised by Piotr Rudawski, Bastian Manschwetus and Per Johnsson

Department of Physics
Division of Atomic Physics
May 2015

Master's Thesis

A high-order harmonic pump-probe setup using annular-beam interferometers

Author:
Hampus Wikmark

Supervisors:
Piotr Rudawski
Bastian Manschwetus
Per Johnsson

Abstract

Demands are specified for an interferometer setup capable of supporting attosecond resolution pump-probe experiments, as well as molecular alignment experiments. A design for two interferometers fulfilling these demands is presented.

As the presented setup relies on annular beams for discrimination, high-order harmonic generation is attempted using annular beams. The success of these experiments as well as calculations performed indicate that this setup will function as intended.

August 8, 2016

Contents

Acronyms

CPA Chirped Pulse Amplification. 15

FEL Free Electron Laser. 3

FWHM Full Width at Half Maximum. 3

HHG High-order Harmonic Generation. 2, 3, 6, 8, 9, 11, 14, 17, 20, 21, 24–27, 30, 32, 41

IR Infrared. ii, 5–8, 14–16, 25, 28, 31–34, 36, 39–41

RABITT Reconstruction of Attosecond Beating by Interference of Two-photon Transitions. 4, 5, 28, 32, 34

SFA Strong Field Approximation. 11, 25

XUV eXtreme Ultraviolet. ii, 2–8, 14–16, 19, 25, 28, 29, 31, 32, 34, 36, 38–42

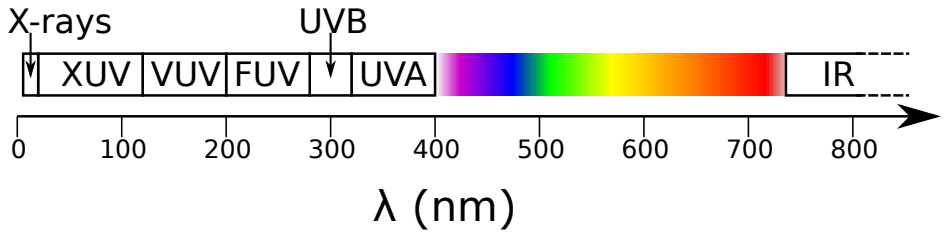

Figure 1: A part of the electromagnetic spectrum, showing Infrared (IR) extending above 700 nm, visible light, UVA and UVB light, Far Ultraviolet (FUV) and Vacuum Ultraviolet (VUV), as well as eXtreme Ultraviolet (XUV) and X-rays.

1 Introduction

The desire to study fast or short-lived phenomena in physics, chemistry and biology has driven the development of measurement methods with higher and higher temporal resolution. For a long time, for example, biologists have taken to using faster and faster cameras to investigate animal behaviors or fast biological processes [1]. These are processes occuring at timescales of milliseconds or microseconds (μs).

In atomic and molecular physics, the interesting phenomena occur at much shorter timescales, down to femtoseconds and attoseconds, as can be seen in Figure 2. The need to study phenomena at these time scales naturally led to the development of new scientific tools.

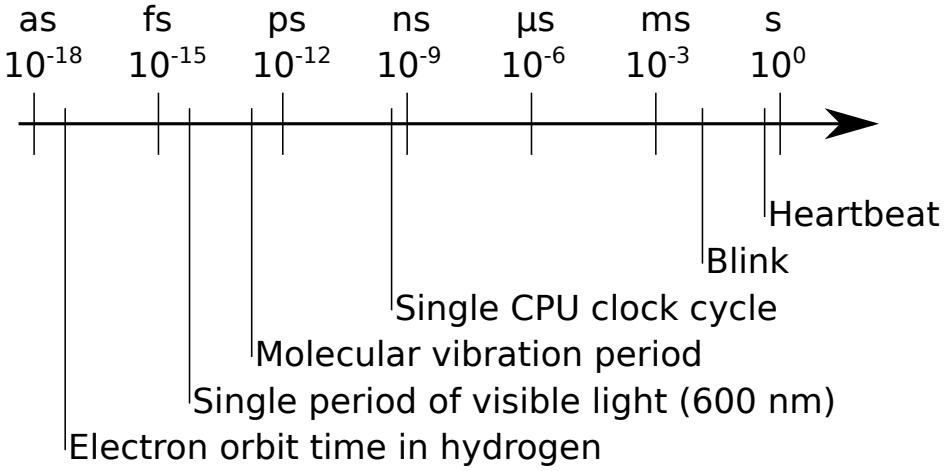

Figure 2: A visualization of the time scales discussed in this thesis compared to more "day-to-day" time scales.

When the laser was developed, its pulses were long-lasting. This was changed with the discovery of mode-locking in 1964 [2], which meant that one could reach pulse lengths down to hundreds of picoseconds.

In the 1980s mode-locking in solid state lasers led to femtosecond pulses [3, 4], which enabled the field of ultrafast optics. The extremely short pulse durations, and thus the high temporal resolution, meant that they quickly found applications in molecular physics and chemistry. The spectroscopic techniques used in this field are applied in medicine, environmental studies and engineering, while providing fundamental scientific insight into the behavior of electrons and charge dynamics in molecules.

Perhaps the most known applications of femtosecond lasers is *femtochemistry*; using femtosecond pulses to observe chemical reactions in real time [5]. With further achievements and decreases in pulse durations, faster and faster processes were resolved.

From 2000 and onwards, physics has seen the characterization and manipulation of attosecond pulses, an order of magnitude shorter than anything possible to produce before [6]. The phenomenon that makes attosecond science possible is known as High-order Harmonic Generation (HHG). HHG describes the process of a strong laser field interacting with a target to produce attosecond pulses in the XUV spectral range.

Just as the revolution of femtosecond lasers enabled new fields of study such as femtochemistry, subfemtosecond pulses open the door to *attoscience*, a new field in the intersection of chemistry, molecular physics and solid state theory.

The unprecedented time resolution offered by attosecond pulses enables resolving electron dynamics within a single atom or molecule, at the very time scale of the movement [7]. One example is to thoroughly investigate light-conductor interactions at the native time of the so-called plasma frequency. This illuminates a number of interesting phenomena such as the reflection of light from a metal surface.

To make good use of these very short time scales it may also be necessary to employ pump-probe experiments, using two pulses whose relative delay can be controlled with very high resolution.

The motivation of this thesis is to design interferometers that can be used for characterization of attosecond pulses and novel time-resolved molecular physics. Several criteria for the properties of this setup are provided and discussed.

A conceptual design for two interferometers is presented, as well as various aspects of the design contributing to the versatility and resolution of the two interferometers.

In the course of development, various challenges were encountered, mainly using annular (ring-shaped) beams for HHG. Therefore, experiments and simulations were carried out to test the feasibility of HHG using annular beams in this context.

1.1 Ultrashort laser pulses

The duration of a pulse with a certain bandwidth is limited to a certain smallest possible number due to the uncertainty principle. This relation is called the time-bandwidth product, and for a Gaussian pulse[1] it can be expressed as [8]

$$\tau_{\mathrm{FWHM}} \cdot \Delta\nu = 0.44, \tag{1}$$

where τ_{FWHM} is the time duration Full Width at Half Maximum (FWHM) in seconds and $\Delta\nu$ is the bandwidth in Hz.

One can deduce from the equation that to have a pulse shorter than a femtosecond one needs to have a bandwidth of more than 440 THz. At 550 nm, the frequency of green light, this corresponds to a wavelength greater than the entire visible spectrum. Thus, in order to make a shorter pulse one needs to increase the central frequency or, equivalently, decrease the central wavelength [6].

The most common sources of short-wavelength radiation (XUV and X-rays) are synchrotrons and Free Electron Lasers (FELs). However, this does not necessarily correspond to shorter pulse lengths. The shortest pulse length achievable with a synchrotron is in the range of 10-100 picoseconds [9]. FELs can have shorter pulse lengths, but not shorter than a few femtoseconds [10]. In this case one does not simply need a large bandwidth, but also for the whole pulse to be coherent.

To create radiation with wavelengths in the XUV and X-ray ranges, it is not possible to use ordinary laser media anymore. One possible way of doing it, however, is to produce this radiation indirectly from a femtosecond laser pulse, using the HHG process [6].

In HHG, short-pulse lasers are used to create extremely strong electric fields on solid surfaces [11] or in gas targets [12], so strong that electrons in the target atoms are stripped from their host atoms and driven back and forth in the fields. If the electrons recombine with the host ion, they have acquired a surplus of kinetic energy which they lose as radiation [13]. A more thorough treatment of HHG, follows in the next chapter.

Attosecond pulses have wavelengths in the XUV and soft X-ray regimes which enables atomic and molecular experiments similar to some of those performed at synchrotrons and FELs [14].

At the time of writing, generated attosecond pulses do not reach the same

[1] A pulse whose temporal profile is described by a Gaussian function.

high photon energies as these large facilites, but are easier and cheaper to make, and is the only measurement tool to feature attosecond resolution [15].

When considering applications of attosecond pulses, it is important not only to be able to create them, but also to examine them, for example to verify that they are in fact as short and broadband as one would want them to. For experiments at these minuscule time scales, there are no electronics fast enough to measure the results.

One method of measuring pulse characteristics, for example the temporal structure, is Reconstruction of Attosecond Beating by Interference of Two-photon Transitions (RABITT) [16]. As the name suggests, the interference between different transition paths is investigated by an IR and an XUV photon [17].

Another measurement technique useful for these ultrashort pulses is streaking [18]. In this scheme, the trajectory of an electron ionized by an attosecond pulse can be changed by an intense longer-wavelength laser field to determine the duration and chirp of the pulse [19].

1.1.1 Pump-probe experiments

The RABITT and streaking techniques mentioned earlier can be seen as types of pump-probe experiments [20]. The common approach is to use two pulses of light, a *pump* to instigate the reaction one wishes to investigate, and a *probe* to see the results.

An example can be an experiment to know the relaxation time of a given electron energy level, in which one may first use a pulse to excite the electron to the level and then another to check whether or not it remains there.

Pump-probe experiments are practically realized in interferometer setups. Very short time scales can thus be measured and manipulated in space (for example, regulating the delay between two pulses by moving mirrors in an interferometer). In a femtosecond, for example, light will travel 0.3 μm, which is orders of magnitude larger than the resolution of modern equipment such as piezoelectric translation stages [21].

In order to measure transitions and levels in larger systems than atoms (i.e. molecules), the pump-probe approach may not be sufficient. Take an organic molecule such as an amino acid. It has a multitude of carbon atoms, so it would be very helpful to know from where in the molecule one ionizes electrons, for example.

1.1.2 Molecular alignment experiments

In order to achieve a "reference frame" to investigate molecular dynamics, it is helpful if the relevant axes of the molecules are aligned with the polarization of the pumping and probing fields. This method is known as molecular alignment [22].

The two main approaches to molecular alignment are adiabatic and nonadiabatic alignment. In an adiabatic scheme, the pulse duration τ is greater than the rotational period τ_{rot} (typically on the picosecond to microsecond scale), and the target molecules are aligned with the laser field as long as it is turned on.

In a nonadiabatic alignment scheme, $\tau < \tau_{\text{rot}}$ and the molecules are instead given an angular momentum increase that causes them to rotate in and out of alignment. This is most efficient if $\tau \ll \tau_{\text{rot}}$, when the molecules can be assumed to effectively stand still during the time of the pulse. This means the alignment pulse should preferably be on the femtosecond time scale [22].

1.2 Design concept

The goal for this thesis is to design a setup for molecular physics experiments, for use at the intense high-order harmonic generation beamline of the Lund Laser Centre. With some modifications, the design may also be used at a future beamline at the ELI-ALPS (Extreme Light Infrastructure - Attosecond Light Pulse Source) facility, currently under construction in Szeged, Hungary.

It is deemed that the design needs to deliver three beams into a molecular target; an IR pulse to align the molecules (henceforth known as the *alignment pulse*, as well as an IR and an XUV pulse to perform attosecond-scale pump-probe experiments.

The IR pulse used for the pump-probe experiments is the attenuated fundamental IR field used in the generation, and thus it will be referred to as the *generation pulse* up to and including the generation process, and the *probe pulse* in pump-probe experiments. Figure 3 on the next page shows a rough sketch of these three beams and their origins.

There are a number of features desired for this type of interferometer setup. Firstly, a few-attosecond resolution of the delay between the pump IR pulse and the XUV probe is required for RABITT and other pump-probe experiments. Secondly, in order for the molecules to align before the experiment, it should be possible for the alignment pulse to come up to 100

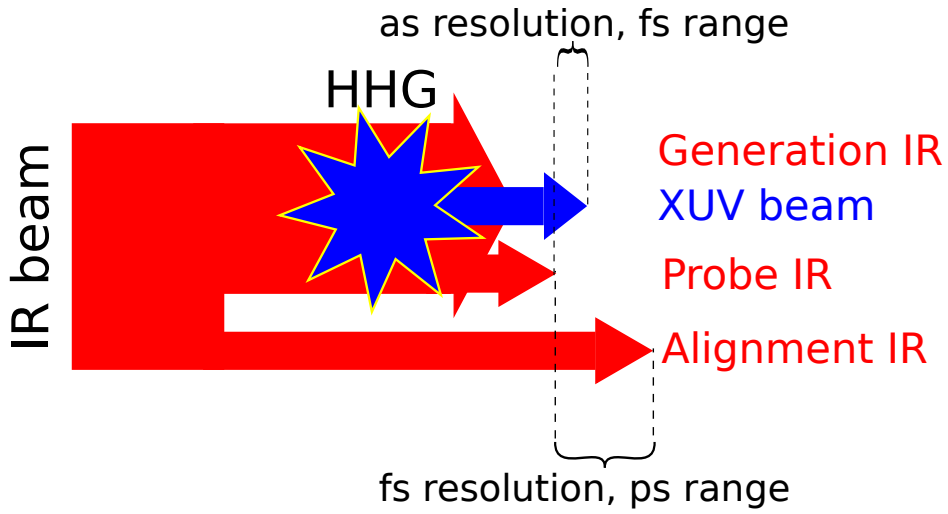

Figure 3: An explanation of the beams that will be discussed in the thesis and the timescales on which one wants to manipulate them.

ps before the pump IR and XUV pulses.

Because of the two different ranges of delays needed, it was not possible to achieve them both at the same time, but instead two interferometers were designed.

In this thesis, a setup concept is studied, consisting of two interferometers, which will be referred to as the *pre-generation* and *post-generation* interferometers, as they are inserted into the beamline before and after the HHG medium, respectively. Section 3 on page 28 will go more in detail regarding the beams and stages involved.

The pre-generation interferometer consists of two mirrors with holes drilled through the center, which enables extraction of a small amount of the pulse energy to be used for the alignment pulse. The generation pulse then becomes an *annular* (ring-shaped) beam.

The alignment pulse can be moved up to 100 ps forward in time by the use of a translation stage, which ensures that most molecules can be adequately aligned.

The post-generation interferometer also depends on bored mirrors, but at grazing angles[2]. These mirrors let the central part of the beam, which contains most of the XUV radiation, through their center, while reflecting

[2]Grazing angles refer to angles shallow to the surface.

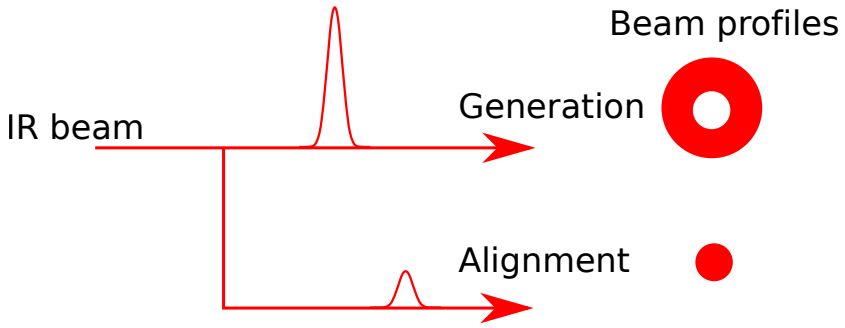

(a) The beams in the first interferometer.

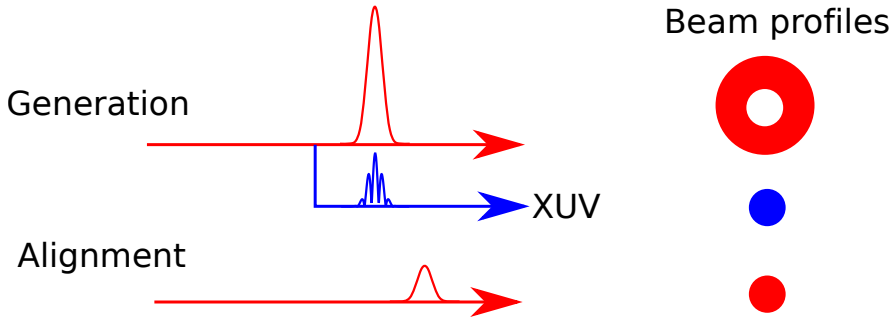

(b) The beams in the process of high harmonic generation. Note that the intensity of the XUV pulse is highly exaggerated.

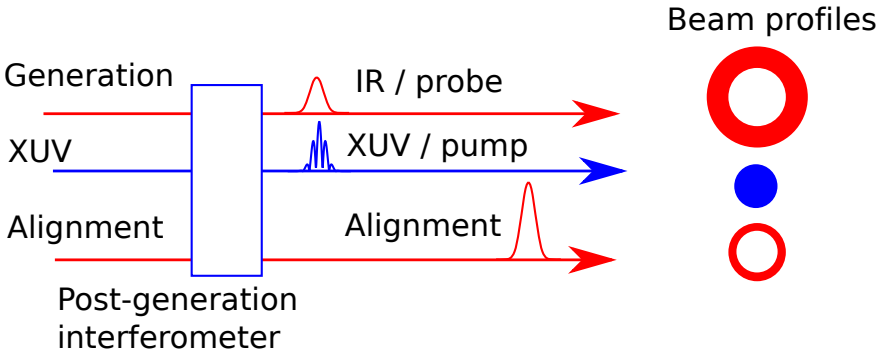

(c) The beams in and after the second interferometer.

Figure 4: An illustration of the beams as they travel through the planned setup. The height of the pulses roughly corresponds to the pulse energy.

both IR beams onto germanium polarizing mirrors at large incident angles. The mirrors are set on a piezo-driven translation stage.

With the help of this stage, it is possible to regulate the delay between the generation IR and the generated XUV pulse with a resolution of less than 30 attoseconds and a range of several picoseconds.

Figure 4 on the previous page shows the spatial characteristics of the resulting beams, as well as their relative intensitites at certain points in the beamline.

1.3 Thesis structure

A key part of the design of the proposed interferometers is the use of annular beams, and thus it is important to know whether the HHG process is perturbed when using annular beams.

The next section, "High-order harmonics using annular beams", will therefore give a brief introduction to the theory on high-order harmonic generation, followed by the experiments and simulations performed to judge the possibility of using annular beams in the context of the process.

Following this, the section on interferometer design provides an introduction to interferometry and the necessary characteristics for the design of the two interferometers.

Finally, a conclusion and outlook is provided, reflecting upon the setup and the possibilites and limitations of the interferometers designed.

2 High-order harmonics using annular beams

2.1 High order harmonic generation

High order harmonic generation describe the process of a strong laser field, incident on a target, generating a pulse of harmonics, that is, fields with frequencies that are multiples of the original field frequency [23].

High-order harmonics typically describe harmonics several times higher than the original frequency. This is normally achieved with a gas target and a generation laser intensity on the order of 10^{14} W/cm^2.

The intensity can be approximated as

$$I \approx \frac{P}{A} = \frac{E}{\tau_{\text{FWHM}} A} \tag{2}$$

where P is the pulse peak power averaged over the area A, E is the pulse energy and τ_{FWHM} is the duration of the pulse. Thus extremely high intensities like this can be achieved through a combination of small focusing areas (a few μm^2), high pulse energies (more than a mJ) and short pulses (tens of femtoseconds).

A characteristic feature in HHG is the harmonic spectrum, as can be seen in Figure 5 on the following page, in which one may see strong low harmonics, a *plateau* in which the harmonic intensity is largely unchanged, and then a rapid cutoff, the energy of which can be approximated to

$$E_{\text{co}} = I_p + 3.17\ E_p \tag{3}$$

where I_p is the ionization potential of the target and E_p is the so-called ponderomotive energy. It represents the average energy given by the laser's electric field to the electron, and can be calculated as [24]

$$E_p = \frac{e^2 E_0^2}{4 m_e \omega^2} \tag{4}$$

where E_0 is the amplitude of the electric field and ω is the frequency.

Figure 5 on the next page shows the typical shape of the harmonic spectrum, with the ionization potential and typical cutoff energy for HHG in argon.

High harmonics can be explained semi-classically using the three-step model [23] and more in-depth using the strong field approximation [20].

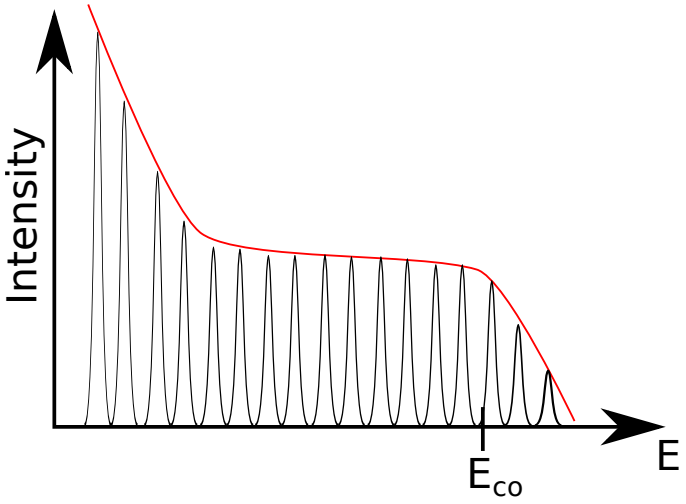

Figure 5: A mockup of a typical harmonic spectrum.

2.1.1 Three-step model

The *simple man's model* or three-step model is an intuitively easy explanation for high-order harmonic generation, the utility of which was proved by its predictions regarding the harmonic energy cutoff [20].

As the name implies, the model proposes three steps to harmonic generation, illustrated in Figure 6 on the following page:

1. The strong E-field of the laser beam distorts the atomic potential so that an electron tunnels out of it.

2. The electron is accelerated by the fluctuating E-field, and turns back towards the atom when the E-field switches directions.

3. The electron recombines with the atom, releasing energy in the form of a photon, the energy of which depends on the potential as well as the kinetic energy the electron acquired in the continuum.

The cutoff energy can then be calculated from the ponderomotive energy by letting an electron propagate in a sinusoidal laser field.

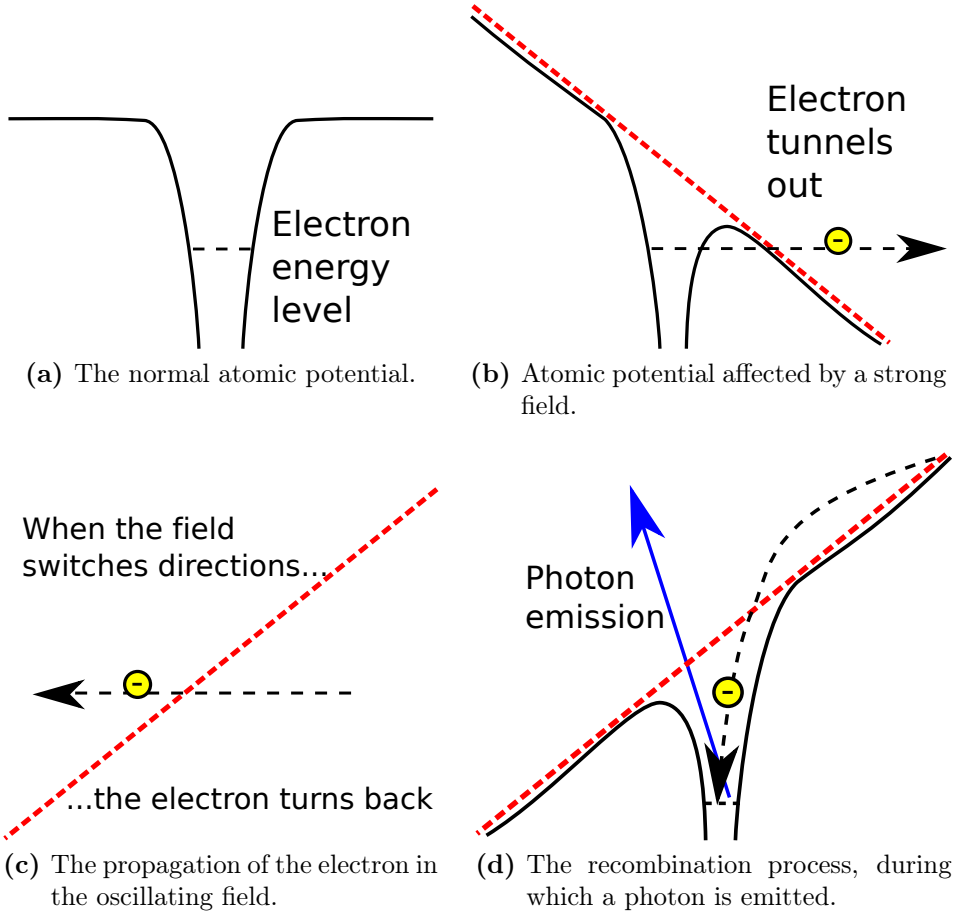

(a) The normal atomic potential.

(b) Atomic potential affected by a strong field.

(c) The propagation of the electron in the oscillating field.

(d) The recombination process, during which a photon is emitted.

Figure 6: An illustration of the three-step model, adapted from [23].

The Strong Field Approximation (SFA), first proposed by Lewenstein et al [13], is a quantum mechanical approach to HHG that gives a more detailed view than the three-step model.

The model is derived from solving the relevant quantum mechanical equations under a few assumptions:

- Only a single electron is considered
- Only electrons from the ground state are ionized, i.e. electrons in higher excited states are neglected.
- The ground state will not be depleted by ionization.

- When the electron is propagating in the laser field, the atomic potential of the parent ion is neglected.
- As the electron recombines with the parent ion, the influence of the laser field is neglected.

The interaction between the laser field and the electron can then be calculated using the time-dependent Schrödinger equation (TDSE) as the interaction of the dipole moments of the atom and the field. Using the saddle-point method, this can be done analytically, greatly saving computing power [20].

2.1.2 Spectral and temporal characteristics

In an isotropic medium such as a gas, the direction of the electric field does not matter, only the amplitude and phase [23]. This means that for each period of the oscillating fundamental field, two points give rise to identical but opposite field ionization properties. Figure 7 shows two identical points separated by half a period.

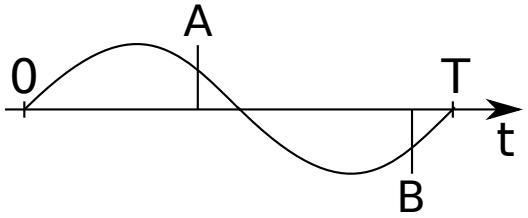

Figure 7: The electric field as a function of time, from [23]. Points **A** and **B** experience the same absolute electric field amplitude, but in opposite directions.

This amounts to a periodicity of $T/2$, where T is the fundamental field period (for a 800 nm laser $T = 2.67$ fs). A periodicity of $T/2$ corresponds inversely to a periodicity of 2ω in the frequency domain.

Odd harmonics are favored over even harmonics because of the mentioned isotropy of the medium; a second-order process ($\chi^{(2)}$) will give a contribution to the polarization of the medium as

$$P(E) = \chi^{(2)} E^2 \tag{5}$$

whereas the π phase shift between points t_1, t_2 separated by a half-cycle (such as A and B in Figure 7) means that

$$P(E(t_1)) = -P(E(t_2)) \tag{6}$$

It can easily be seen that the only solution to both of these equations is that the nonlinearity is 0. This is true for any even-order process. Thus one will see only odd harmonics, unless one perturbs the field periodicity [23] or uses a non-isotropic medium.

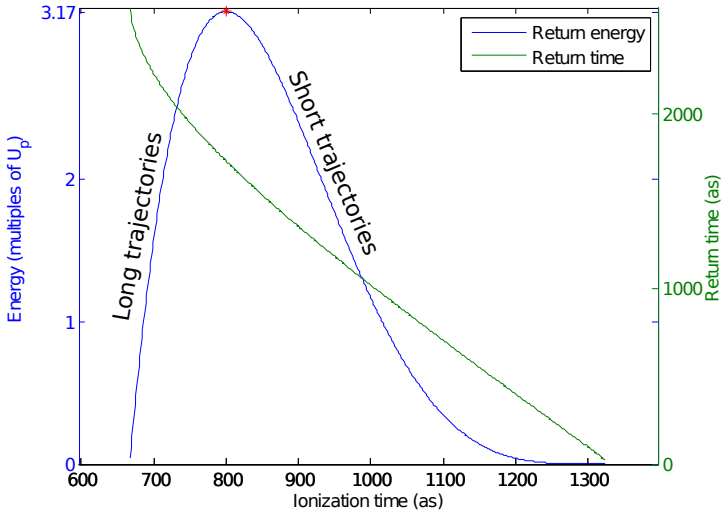

Figure 8: The return time and collected energy of the electron as a function of when it leaves the atom, from [23].

Figure 8 shows how the point in each half-cycle at which the electron leaves the atom affects the energy it gathers in the continuum, as well as the time it takes for it to return. As can be seen, at a certain point the electron has reached the cutoff energy. Electrons that leave before and after this point are said to folllow the long and short trajectories, respectively.

Harmonics are emitted as a "pulse train" of short attosecond pulses, which corresponds to the characteristic spectrum of separate harmonics. If one isolates a single one of these pulses, its spectrum will be continuous and broadband [25].

2.1.3 Macroscopic effects

So far only the *single-atom response* has been considered. This considers the effect the field has on only one atom in the medium. When one considers the entire generation medium, however, the picture becomes more complicated, mostly due to phase matching.

If the emitted harmonics are not in phase with the generation field, the resulting *wave vector mismatch* will cause destructive interference and thus a reduction in harmonic yield. This mismatch can be expressed as [25]

$$\Delta\vec{k} = \Delta\vec{k}_g + \Delta\vec{k}_d + \Delta\vec{k}_n + \Delta\vec{k}_p, \tag{7}$$

where each vector is the contribution to mismatch from one factor; $\Delta\vec{k}_g$ from the Gouy phase shift[3], $\Delta\vec{k}_d$ from the dipole phase shift and $\Delta\vec{k}_n$ and $\Delta\vec{k}_p$ from dispersion in neutral atoms and plasma, respectively.

At the conditions of the performed experiments (comparatively low generation medium pressure, and long focusing length), $\Delta\vec{k}_d$ is the dominant component [23]. This contribution varies strongly with both z and x (on-and off-axis position) and thus has a larger impact on the long trajectories (since those electrons propagate for a longer distance). Because of this, the short trajectories are generally the most important component in the resultant harmonics.

2.2 Annular beams

Annular, or ring-shaped beams, can be used for various purposes regarding discrimination and interferometry [26, 17].

Normal ways of making annular beams is using holey mirrors, which will transmit an annular beam and transmit a small, regular beam [27], and blocking the center of the beam with an opaque object [26].

Just after making the beam annular, it can be pictured quite simply as the old beam profile except with the intensity 0 around the center, to the extent of the hole or block. In the focus, however, this is replaced by a faint fringe pattern.

Figure 9 on the following page shows a somewhat simplified picture of the focus, simply the Fourier transform of an annular beam and a regular beam. The fringe pattern can be seen somewhat, but it is apparent that the central focus feature is very similar between the two. This characteristic can be exploited in the context of HHG; since the intense center component will drive almost all generation, an annular IR driving field will generate a non-annular XUV beam [26].

[3]The Gouy phase shift is characteristic of a Gaussian beam and denotes a phase shift of π along the length of the beam across the focus.

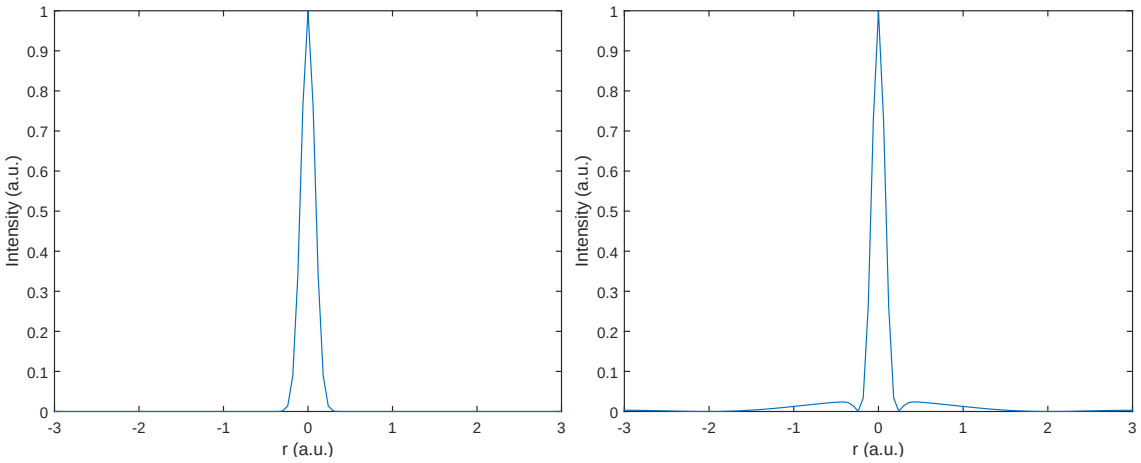

(a) Regular beam. **(b)** Annular beam.

Figure 9: The focal profiles of regular and annular beams.

2.3 Experiments on HHG with annular beams

2.3.1 Intense HHG Beamline

All experiments for this thesis were carried out at the Lund Laser Centre intense harmonic beamline [25, 14], the main features of which are shown in Figure 10 on the next page. The beamline is driven by a 10 Hz Ti:Sapphire laser, which it shares with a neighboring beamline used for particle acceleration.

The laser is based on Chirped Pulse Amplification (CPA) in order to obtain short and intense pulses [24]. The resulting pulses are around 35-40 fs long and can have a pulse energy of up to 100 mJ. The beam is enlarged before the compressor, to a diameter of about 30 mm.

To get sufficient intensity for high-order harmonic generation the beam focused by a lens of 8.7 m focal length, and folded using a mirror, for space saving reasons. Before the in-coupling mirror there is also an adjustable aperture. Changing the size of this aperture will alter the f-number of the beam and thus its focal spot size, but also its pulse energy, as one trims the edges of the beam.

The intensities reached by the focused IR beam will create plasmas in any material, and the generated harmonics consist of XUV which is absorbed strongly in air. Therefore, the whole setup after the coupling mirror is pumped to a high vacuum (about $10^{-6} - 10^{-8}$ mbar).

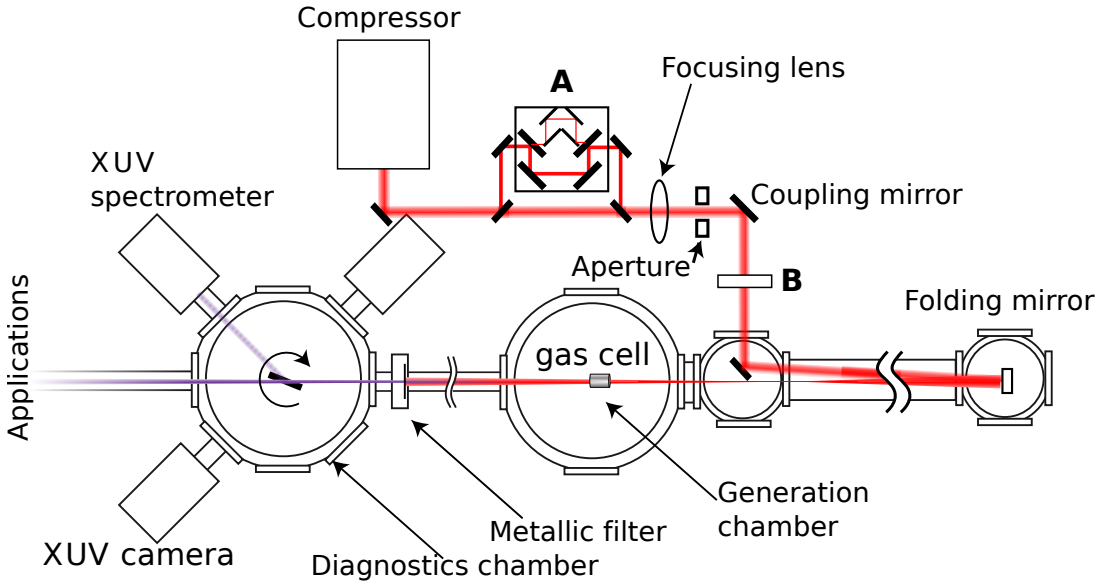

Figure 10: A sketch of the intense harmonic beamline setup, adapted from [25].

The focus of the beam is in the generation chamber, in which the gas cell is marked. As the gas cell position is more or less fixed in the generation chamber, moving the lens along the axis of the beam effectively moves the gas cell in and out of focus. After generation, the XUV and IR beams then propagate collinearly to the diagnostics chamber shown in the leftmost part of Figure 10.

A diagnostics chamber features a rotating mirror to enable guiding an XUV beam to various instruments. The instruments used in the following experiments were an XUV spectrometer and an *ANDOR* XUV camera for imaging the spatial structure of the beam.

In the process of these diagnostics, the IR beam is often blocked with a metallic filter (mostly 1 μm Al) because its high power would damage the sensitive XUV detectors.

In order to perform experiments with annular beams, two approaches were taken. One was to install the pre-generation interferometer, featuring mirrors with 2 mm central holes, at **A** in Figure 10. The other was to put a glass plate at **B** and block the center of the laser beam with metal discs of varying sizes.

2.3.2 Experiments

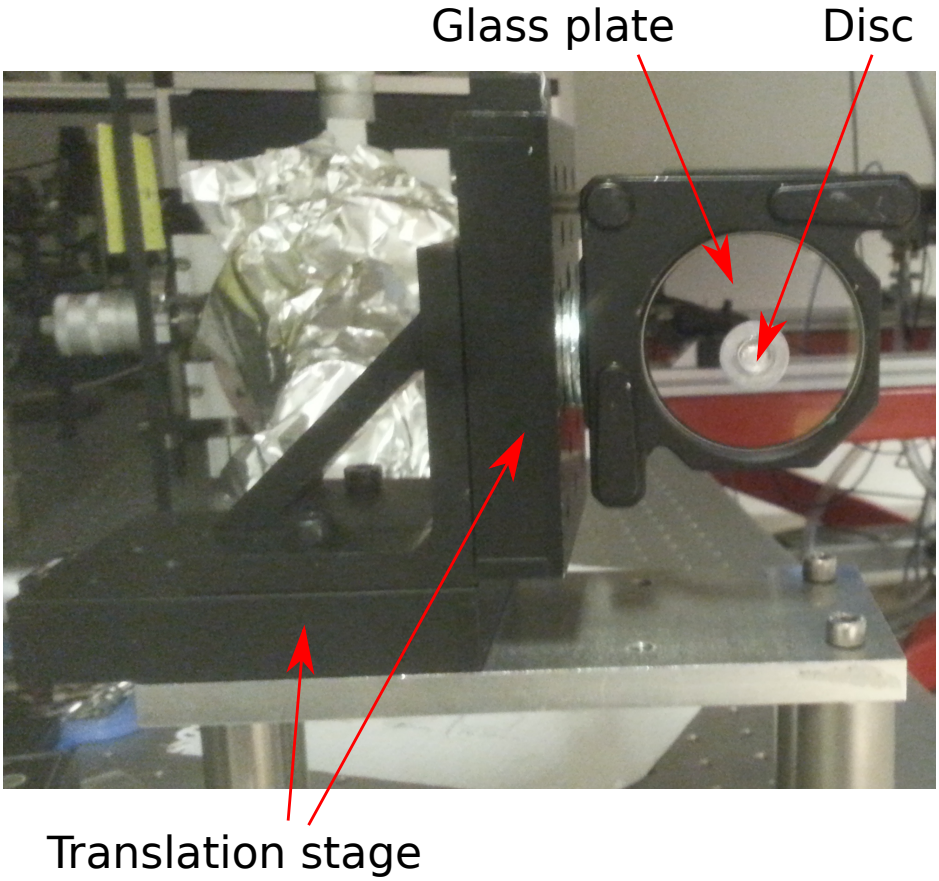

Figure 11: The setup for creating annular beams of varying sizes (**B**).

To investigate the influence of annular beams on HHG, a new system was built, in which the beam was given an annular character by blocking the center of the beam.

This was accomplished by attaching circular metal discs onto a fused silica plate with anti-reflection coating for 800 nm to minimize losses. Figure 11 shows the build of this apparatus.

The discs ranged in size from 4.50 to 16.10 mm and were centered onto the beam by way of a 2D translation stage which is also shown in the image.

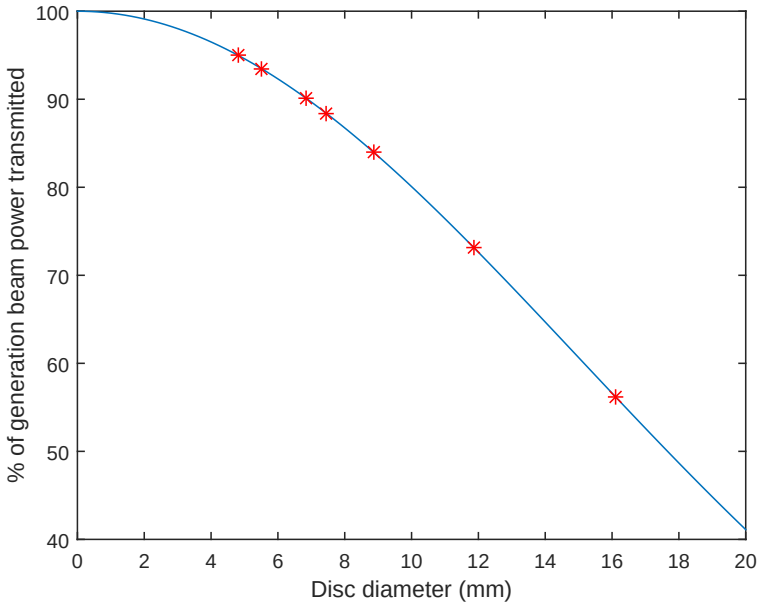

Figure 12: Transmission of generation beam power as a function of disc diameter. The red marks indicate the disc sizes used.

As can be seen in Figure 12, the larger the discs, the more power is lost in the generation beam. Thus, in order to achieve the same pulse energy for each disc size, the largest disc (16.10 mm) was attached, and the maximum laser power after the disc was measured to be 16 mJ. This power was then used for all disc sizes.

In these experiments, a series of measurements were taken using varying disc size, in which one measurement was taken using the same pulse energy for each size, as specified above, and one optimizing the harmonic yield by changing the aperture size and pulse energy. At this point the focusing lens was placed so that the gas cell was approximately 11.5 cm before the focus of the beam.

Then, another scan was carried out for which the lens was moved so that the gas cell was moved 35 cm towards the focus of the beam, meaning that the gas cell ended up 23.5 cm behind the focus instead. In this case, only optimized conditions were measured.

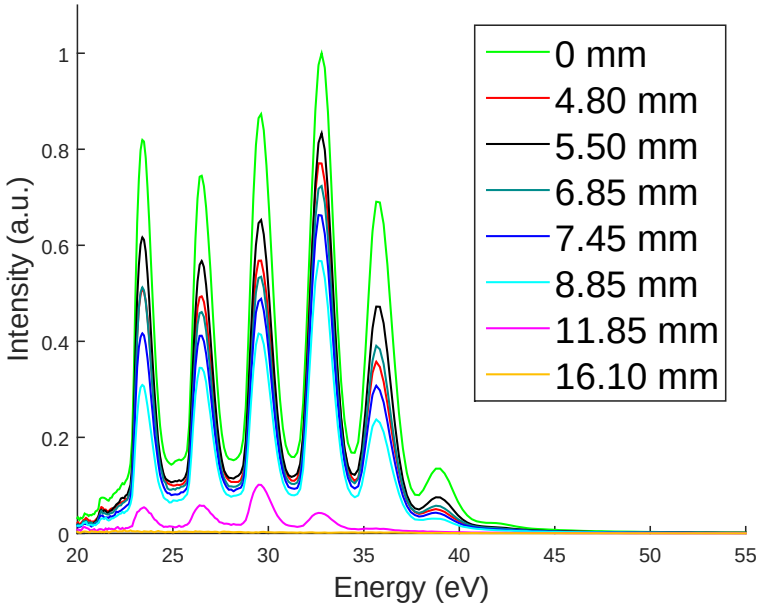

Figure 13: The collected spectrum of the disc-size scan, non-optimized and 11.5 cm from the focus, for the same pulse energy (16 mJ) every time. The legend shows the size of the annularity introduced.

Figure 13 shows the spectra taken with different disc sizes at the same conditions (21 mm aperture opening and about 16 mJ pulse energy, with the gas cell close to the focus). As can be seen in this plot, there is a reduction in harmonic yield for all discs, which increases with the size of the disc.

It appears that somewhere between 8.85 and 11.85 mm there is a quite dramatic drop-off in harmonic yield. For the largest disc, 16.10 mm, it's impossible to discern any harmonic spectrum at all.

While this does indicate an adverse impact of annular beams on the harmonic yield, it is not very dramatic for small hole sizes. The peak XUV intensity for the 5.50 mm annular beam is at 83% of that of the regular beam (0 mm).

Figure 14 on the next page shows the spectra for the same disc sizes as before, but this time attempts were made to optimize generation conditions. For most of the measurements this was done by increasing the iris diameter from 21 to 24-26 mm and adjusting the pulse energy between 35-45 mJ. A few comparisons can be made between this spectrum and the previous one.

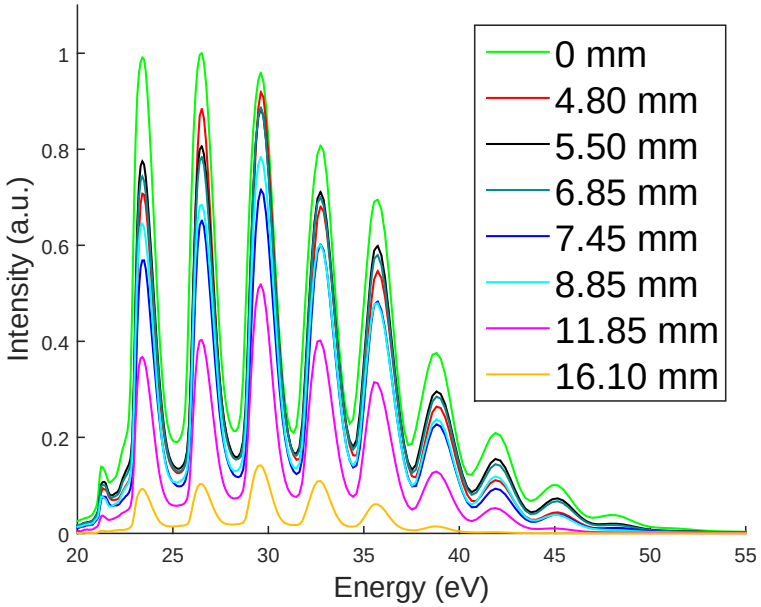

Figure 14: The collected spectrum of the disc-size scan, 11.5 cm from the focus, while optimizing conditions with respect to iris diameter and pulse energy. The legend shows the size of the annularity introduced.

It appears that the detrimental influence of large-hole beams on HHG can be compensated somewhat by optimizing these conditions. Even the beam with a 16.10 mm central hole gives a noticeable HHG spectrum, and 11.85 mm central hole (almost half the diameter of the beam), which previously only showed up somewhat, has around 50% of the intensity of the beam with no annularity.

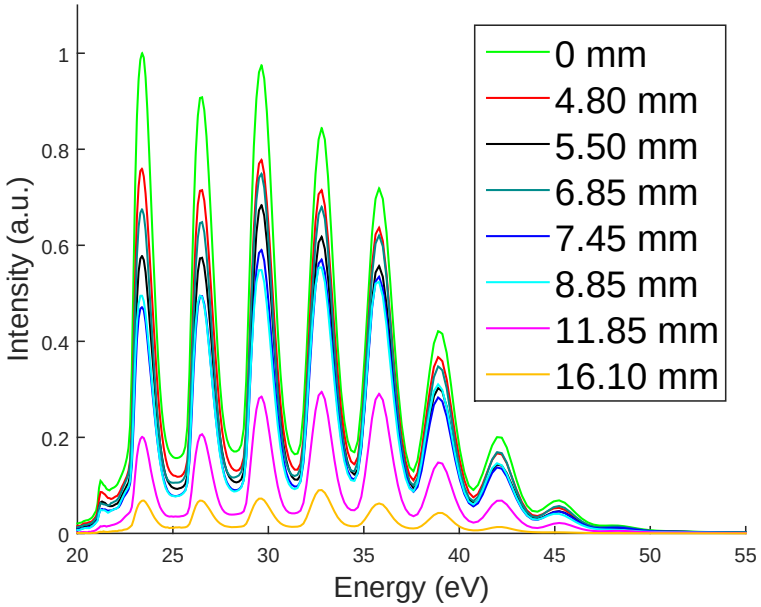

Figure 15: The collected spectrum for a measurement 23.5 cm from focus, with optimized conditions with respect to iris diameter and pulse energy. The legend shows the size of the annularity introduced.

Figure 15 shows the measurements taken at the new position, 23.5 cm behind the focus. For these measurements, the energy and aperture size were changed to a greater extent than the previous measurement with optimized conditions (41-53 mJ and 21-29 mm, respectively).

The results of these measurements shows something in between the two previous measurements. The annular-beam HHG seems more efficient with the optimized conditions here than in the unoptimized conditions shown in figure 13 on page 19, but less so than the optimized conditions closer to focus shown in figure 14 on the preceding page.

Figure 16 on the next page shows a summary of the results of these three measurement series, as a function of the disk size, with the first measurement denoting the unoptimized signal, the second the optimized signal close to focus, and the third the optimized signal further from focus.

The top plot clearly indicates the trend of falling integrated HHG signal with increasing disc size, although this is most pronounced for the unoptimized case (using the same aperture diameter and pulse energy).

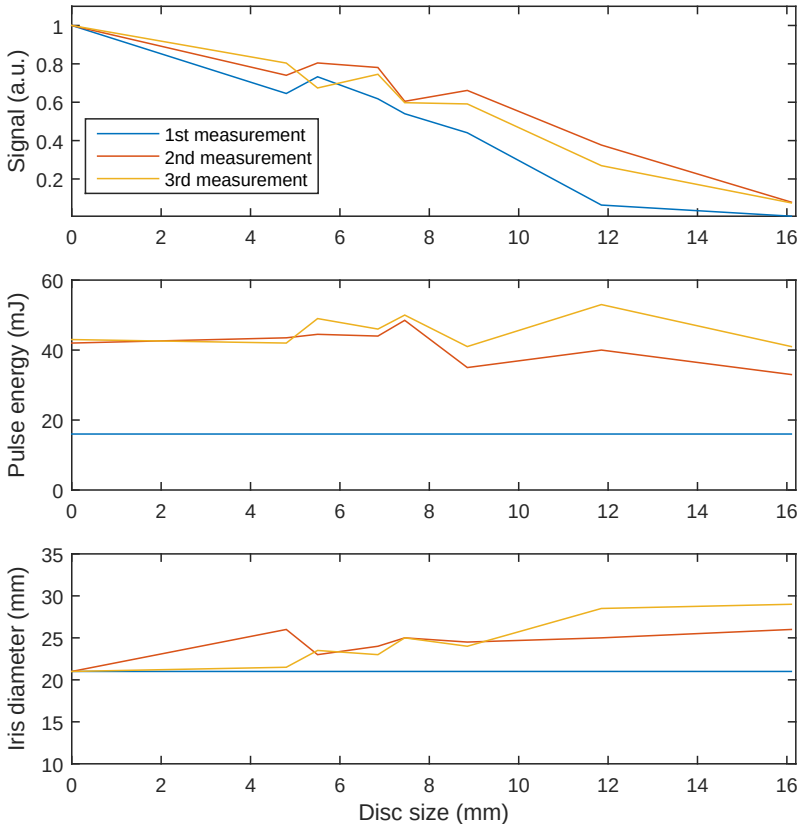

Figure 16: The conclusion of the three mentioned measurement series for the disc-size scan experiment.

The middle plot shows the pulse energy used in the measurements. For the first series, it is 16 mJ for each point. For the two others, there is some slight variations but seems to be no clear trend.

The bottom plot shows the aperture diameter used. Here one can see a trend towards larger aperture openings, which seems reasonable given that one may need to use a larger part of the beam when the center is blocked.

Another series of measurements were taken, using the pre-generation interferometer (shown in Figure 17). For this experiment, the alignment arm was blocked and thus only the annular beam was transmitted.

The holey mirrors are silver coated and have a central hole of 2 mm size. A set of detachable mirrors were used to route the beam into the interferometer, placed at **A** in Figure 10 on page 16, and a scan over several positions of the focusing lens in relation to the coupling mirror was performed with and without it.

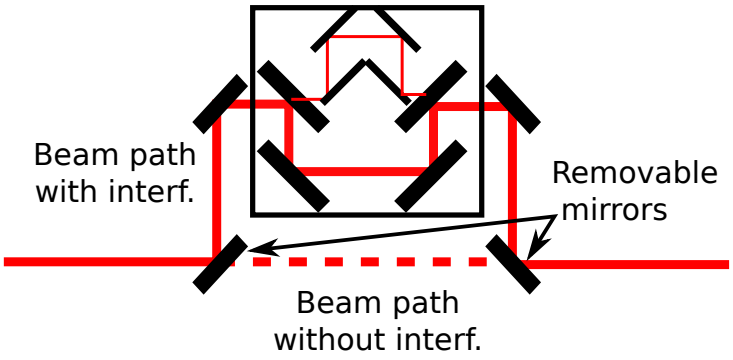

Figure 17: The beam path with and without the pre-generation interferometer.

At the time of this experiment, the folding mirror had been moved out so that the folding length was around 50 cm longer than in the previous experiment due to a changed divergence in the beam, meaning that the gas cell was further from the focus.

Two modes of investigation were chosen; to look at the spectrum in as similar conditions as possible, and to try to optimize conditions with and without the interferometer.

The harmonic spectra with and without the interferometer can be seen in Figure 18 on the following page. The lens was in the same position with and without the interferometer, and the pulse energy was measured to be slightly higher in the interferometer beam (26.2 mJ versus 25.7 mJ). As can be seen, the harmonic signal is still much weaker.

The harmonic spectra, in the respective optimum conditions for the case of using and not using the interferometer, can be seen in Figure 19 on page 25. As can be seen in the plot, the insertion of the interferometer causes a drop in both harmonic flux and cutoff energy, with the ”peak” harmonic being about two harmonic orders lower, and the peak flux about 16 times lower.

The likely explanation for the results of these out-of-focus experiments is that the effect of annular beams increases as one moves generation further

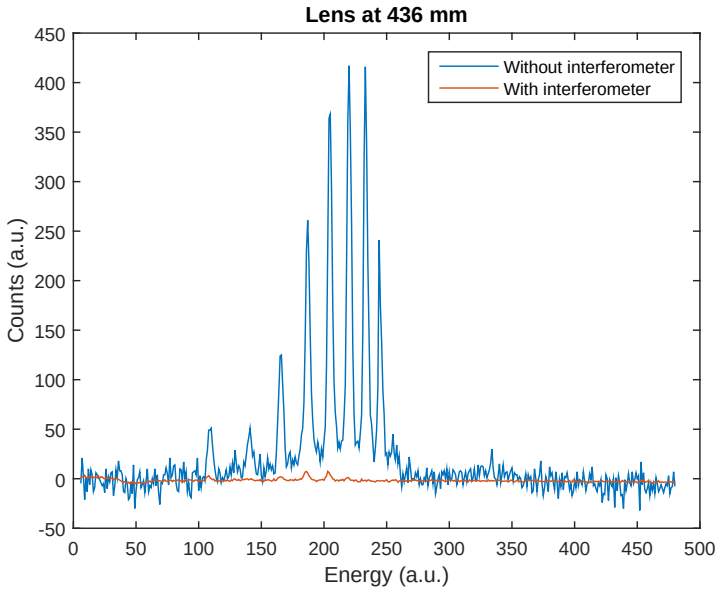

Figure 18: The harmonic spectrum with and without the interferometer, with as similar conditions as possible in lens position and pulse energy.

from the focus of the beam. Intuitively this explanation makes sense, since it's assumed that annular beams look similar to non-annular beams in the focus and they obviously do not in the far-field. This could also explain why HHG with annular beams is more efficient when the lens is such that the generation takes place closer to focus, as in Figure 19 on the following page.

This is further corroborated by the disc-size scan measurements. In these, with optimized conditions, HHG was more adversely affected by annular beams as the measurements were moved further from the focus.

The results are more dramatic in these later experiments, but this could also be due to unknown effects of the different divergence of the laser at the time of measurement.

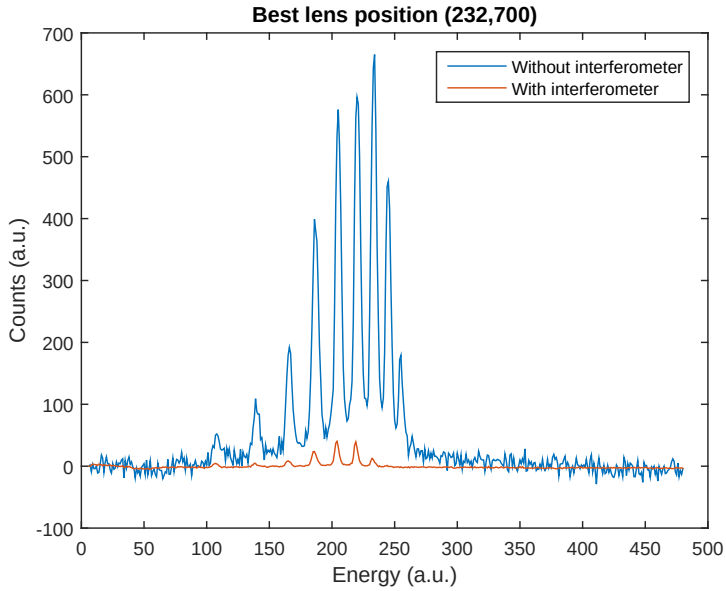

Figure 19: The harmonic spectrum with and without the pre-generation interferometer, at the respective best lens positions, separated by about 470 mm.

2.4 Simulations

To verify the results of the experiments, a number of simulations were performed. First, the propagation of annular and non-annular beams was calculated using Photon Engineering's FRED software. Then, the wavefronts were extracted at and close to the focus, and used for simulations of the HHG process.

The program used for these simulations was a modified version of code previously used for example in [28]. It splits a pulse up into pieces in time, and lets each "slice" propagate through the generation medium.

At each point in the propagation, the electric field amplitude and phase is calculated for both the generation IR and for the generated XUV field, using experimentally measured ionization rates and the SFA.

Figure 20 on the next page shows the simulated spectrum for a few harmonic orders, calculated using this combination of softwares with initial conditions chosen to be as close at possible to the experiments. This assumed two Gaussian beams with 30 mm diameter, with the same pulse energy of 50 mJ, but one of them having a 5 mm hole in the center. Both beams were

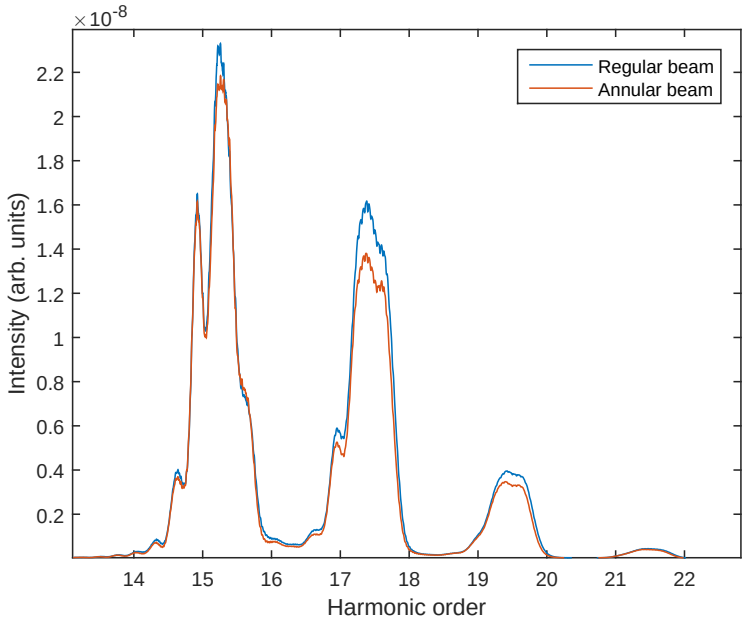

Figure 20: A sample output from the simulation software, showing the harmonic spectrum for a few harmonic orders, for the regular and annular beam.

then focused in a lens with 8.7 m focal length.

Notably, while the experiments concerned generation in argon, for software reasons the simulations were performed on xenon gas. Thus results could only be compared qualitatively between simulation and experiment.

The simulations do, however, agree with the experiments, showing a slight decrease in harmonic intensity. This is interesting because the wavefronts look remarkably similar close to focus. Some radial distance from the center of the focal spot, however, the annularity leads to oscillations in electric field amplitude that presumably perturb the generation in some way. This can be seen in Figure 21 on the following page.

Since HHG is such a nonlinear process, any small change in amplitude or phase of the generation field may lead to dramatic differences in generation.

Differences between the simulation and experimental results of the propagation of the IR beams may be explained by the fact that the simulated beams have an ideal shape as Gaussian beams, and are not affected by any irregularities in shape and consistency which may change the actual beam.

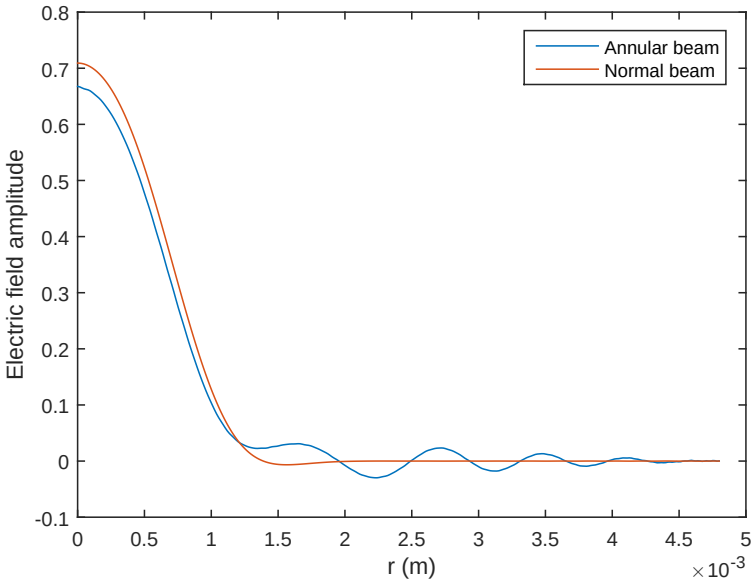

Figure 21: A cross-section of the two IR beams at the first focus.

2.5 Conclusions of annular beam tests

The experiment performed closest to focus seems to indicate that, for a reasonably small center hole in the beam (judging by the results, about 10-30% of the beam diameter), there's only a slight reduction in harmonic yield, and thus this design is viable.

This is corroborated by the simulation results, showing only a 5-10% decrease in peak harmonic intensity.

Furthermore, high-order harmonic generation using annular beams has been observed before [17, 27], and the labs which use annular beams for other experiments can, in a sense, be considered to also perform experiments in which generation with annular beams is proved succesful and efficient.

However, it is important to note that it seems out of focus HHG is more severely affected by annular beams. Generating out of focus is a way to achieve ideal phase matching conditions, as one can use a larger volume medium to avoid saturating the medium [25], so one must consider that the utility of this is affected by annular beams.

3 Interferometer designs

3.1 Interferometry for pump-probe experiments

Interferometry deals with the measurement of phase differences between waves or beams. A typical simple interferometer is a device that splits a beam up into two components, delays one with respect to the other in a particular way, and recombines them. Simple designs like this include Mach-Zehnder, Michelson, and Sagnac interferometers [8].

Both interferometers discussed in this thesis are designed to introduce time delays between different beams. This delay Δt can be expressed as

$$\Delta t = \frac{d}{c}, \tag{8}$$

where the path length d is the product of the difference in distance travelled Δz and the refractive index n of the medium propagated through.

3.2 Demands for interferometer setup

As mentioned in the introduction, a number on demands were considered when designing the two interferometers:

- To perform molecular alignment experiments as well as XUV-IR pump-probe experiments, the interferometer setup must accomodate two IR beams and one XUV.
- An attosecond resolution of XUV-IR delay is necessary for high-resolution experiments such as RABITT.
- Molecular alignment experiments require a delay range of up to 100 picoseconds between the alignment IR pulse and the following pulses.
- For RABITT measurements, the pump IR field must have approximately the same intensity as the harmonics. For molecular alignment, the alignment field must have an intensity an order of magnitude higher.

3.3 Proposed interferometer setup

Figure 22 on the next page shows the proposed new setup of the intense harmonic beamline. The focusing conditions are unchanged compared to

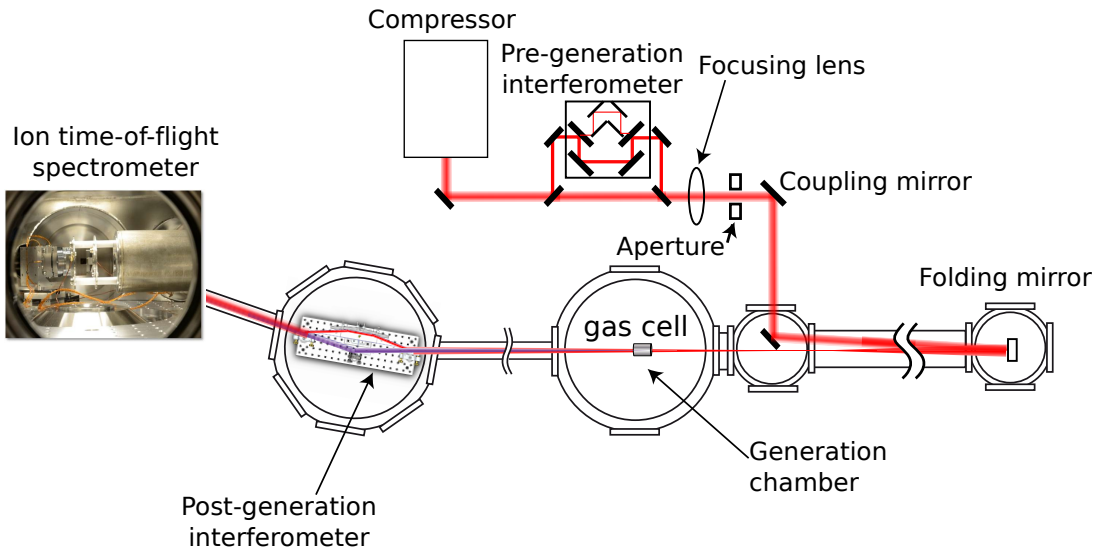

Figure 22: A sketch of the intense harmonic beamline setup, as it will look with the proposed interferometers.

before, the only significant change before focus being the possible inserting of the pre-generation interferometer before the lens.

Notably, the diagnostics chamber will be turned somewhat and the post-generation interferometer will replace the mirror used to direct light to the spectrometers and cameras, as in Figure 10 on page 16.

This also means that the setup will be somewhat "twisted", in that the XUV beam will exit the old diagnostics chamber at an angle of 20°.

A new diagnostics chamber will be constructed, and the beam will finally lead to a time-of-flight spectrometer for ionization measurements.

3.4 Pre-generation interferometer

Figure 23 on the next page shows a sketch of the pre-generation interferometer's design. The design was briefly introduced in the previous section for the preliminary tests of its design, but its utility for molecular alignment will here be explained in some more detail.

In this design, which is a variation of the Mach-Zender configuration [8], the full beam[4], an 800 nm IR laser with a diameter of approximately 30 mm,

[4]The laser setup is more thoroughly discussed in Section 2.3.1 on page 15.

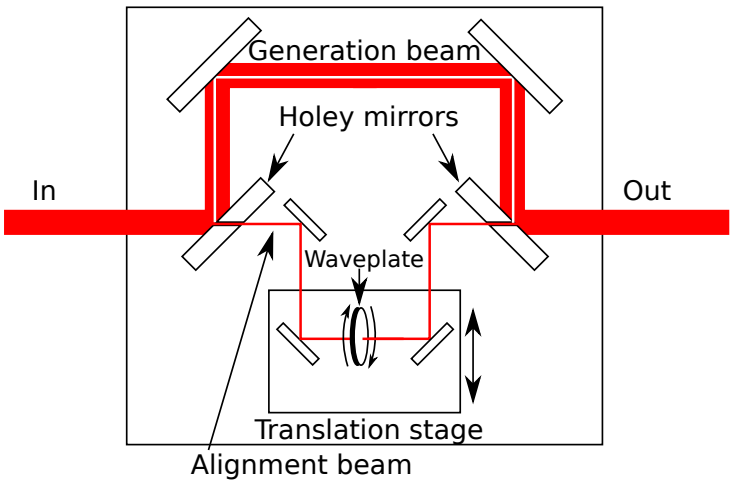

Figure 23: A sketch of the design of the pre-generation interferometer.

enters the interferometer and meets a holey mirror. This is a glass plate with a silver coating, bored through its center at 45° with a hole size of 2 mm.

The holey mirror splits the beam into the annular generation beam and the central alignment beam. The generation beam is simply guided through the interferometer, whereas the alignment beam goes through the holey mirror and is diverted onto a translation stage, driven by a stepper motor. This is to enable automation of alignment-generation delay.

Because of the different sizes of the beams, the generation beam arm uses 2" optics and the alignment beam arm uses 1".

The translation stage has a travel range of about 1.5 cm. Considering the light travels the distance twice, this means the delay range of the interferometer is

$$\Delta t = \frac{3 \text{ cm}}{c} = 1.001 \cdot 10^{-10} \text{ s} \approx 100 \text{ ps}. \tag{9}$$

This delay range ensures that many molecular alignment experiments can be performed.

The translation stage also features a half-wave plate, which can rotate the polarization of the alignment beam relative to the generation beam. Apart from the obvious advantage of using a smaller (and thus cheaper) wave plate, it is also beneficial to generate using s polarization, a fact which will be explained in the next section.

3.5 Post-generation interferometer

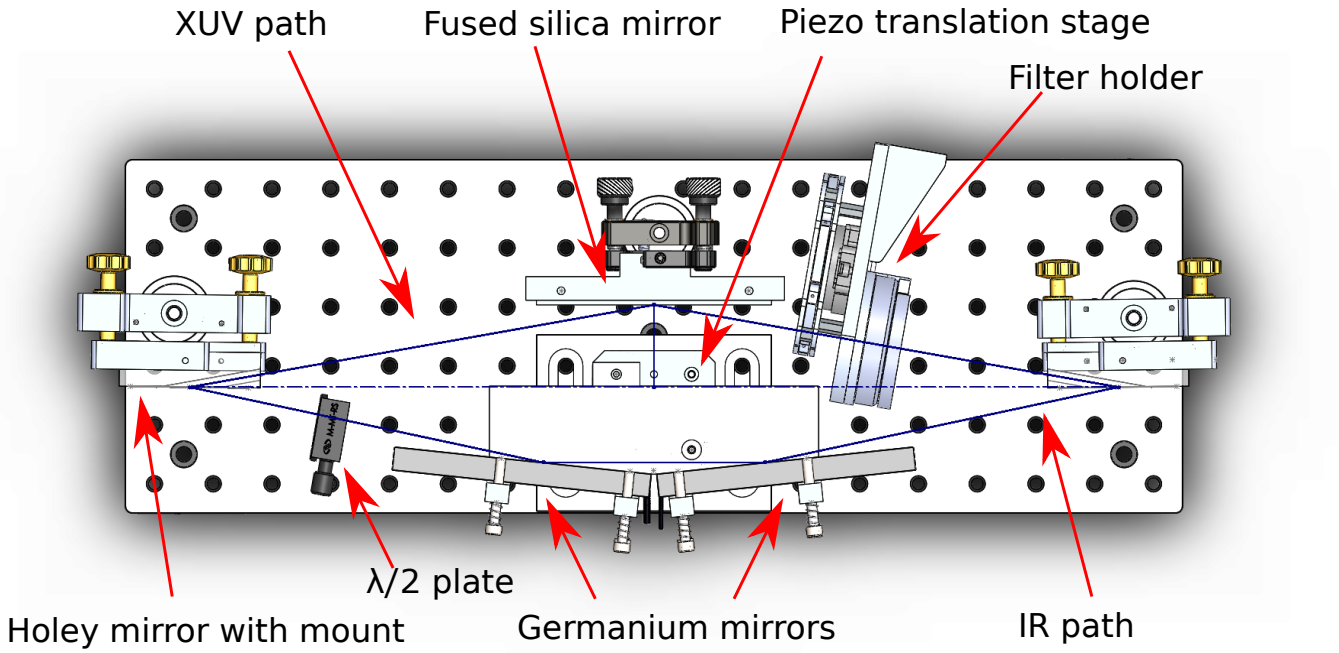

Figure 24: A sketch of the design of the post-generation interferometer.

A sketch of the post-generation interferometer is shown in Figure 24.

The post-generation interferometer is designed to be inserted in what is now the diagnostics chamber of the high-intensity HHG beamline, to compare Figure 10 on page 16 and Figure 22 on page 29.

This design, like the pre-generation interferometer, features a pair of holey mirrors and a translation stage. Here, however, the holey mirrors are used at grazing angles to separate the IR beams from the XUV, leading to the upper and lower path seen in Figure 24.

The XUV beam, along with a residual IR component, is reflected on a fused silica plate which is anti-reflection coated for IR, leading to most IR being transmitted out of the path to the experiment. To ensure that this path contains only XUV, a metal filter removes any remaining IR.

The IR beams (the alignment beam as well as the generation/pump) are reflected on a germanium mirror array designed to attenuate the pump

beam while preserving the alignment beam. These mirrors are mounted on a piezoelectric translation stage that ensures a step size of a few nanometers.

3.5.1 Annular beams

If one considers a Gaussian beam, which has the divergence angle

$$\theta \approx \frac{\lambda}{\pi w_0}, \tag{10}$$

where w_0 is the waist of the beam, it is clear that a beam with the same waist but a much smaller wavelength will have a smaller divergence. Even considering that HHG takes place more in the center of the beam, this leads to the XUV beam having a smaller divergence than the generating field [26].

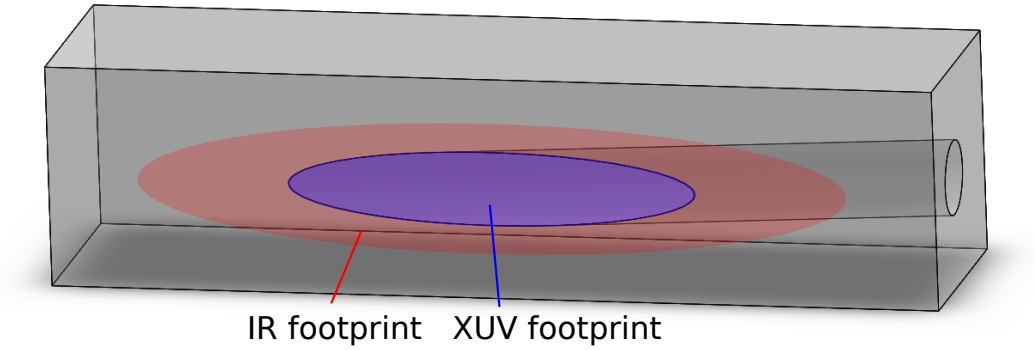

Figure 25: A sketch of the holey mirror design.

Figure 25 shows a sketch of the holey mirrors designed to exploit this characteristic. With the beams arriving at the long face at grazing incidence, this mirror will let through the inner part of the beam (which is most of the XUV) and reflect the rest as an annular beam.

3.5.2 IR-XUV delay

In order to perform pump-probe experiments such as RABITT, the delay between the XUV and IR pulses needed to be on the order of a few femtoseconds, but most importantly the resolution needed to be as high as possible.

The post-generation interferometer design, as can be seen in Figure 24 on the preceding page, relies on only one fused silica mirror for the XUV beam , which at 80 degree grazing angle (10 degrees from the surface) has

a reflectivity of 50-60% in the 30-75 eV range, leading to a total loss of less than 40%.

To make it possible for the IR probe pulse to arrive both before and after the harmonics, it is reflected on two mirrors, and at 12 degrees total incidence angle. The mirrors being wider than the footprint of the beam, they can be moved to shorten or elongate the IR path length. As there are two mirrors at equal but opposite angles, the beam will always end up in the same place, the second holey mirror, at the same angle.

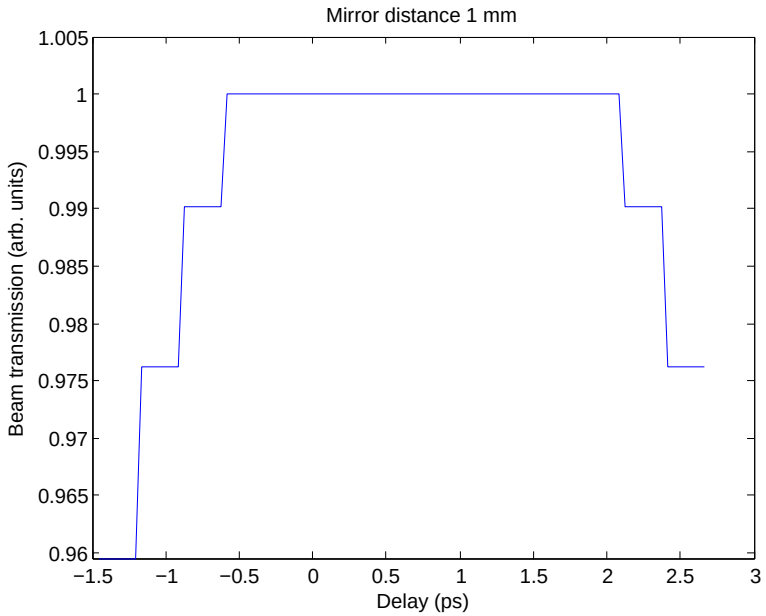

Figure 26: The stability curve, showing the theoretical delay range of the interferometer.

Figure 26 shows the so-called stability curve of the interferometer, which shows to what extent the mirrors can be moved up and down and still reflect the full IR beam.

In order to move the two mirrors, they are placed on a Piezosystem Jena piezoelectric translation stage. Its stated characteristics are a 400 μm scan range, and a 8 nm resolution [21]. Considering the lower path a trapezoid, it can be calculated that changing the height of the trapezoid corresponds to a change in the IR path length with a factor of 0.84, i.e. moving the mirrors 1 μm down will increase the path length by 0.84 μm.

Inserting this factor into Equation (8) on page 28 will yield the delay

range and resolution

$$\Delta t \text{ (Delay range)} = \frac{0.84 \cdot 400 \ \mu\text{m}}{c} = 1.12 \cdot 10^{-12} \text{ s} \approx 1100 \text{ fs}$$
$$\text{and} \tag{11}$$
$$\Delta t \text{ (Resolution)} = \frac{0.84 \cdot 8 \text{ nm}}{c} = 2.245 \cdot 10^{-17} \text{ s} \approx 22.5 \text{ as}.$$

3.5.3 IR-IR discrimination

This setup design lets all beams propagate collinearly through most of the design. Both the alignment beam and the generation beam are focused into the generation chamber together (the first focus), and all three beams (alignment IR, pump IR, and probe XUV) will be focused into a molecular target (the second focus) at the end of the beamline.

This has the advantage that less alignment and adjustment is needed, since many optical components are shared between some or all beams.

The main issue this introduces, however, is a matter of varying needs for pulse energy at different points. In the second focus, in which one wants to perform molecular alignment experiments, the alignment pulse needs to be an order of magnitude stronger than the following IR pulse, when doing RABITT on aligned molecules for example.

However, in the first focus, where generation takes place, it is important that the alignment pulse does not cause harmonic generation, which would disturb the experiments. Thus it must be about an order of magnitude weaker than the generation pulse.

In conclusion, this means that the post-generation interferometer must somehow favor the alignment beam approximately 100 times, compared to the generation beam.

The best way of doing this was deemed to be using polarizers, inserting a wave plate into the pre-generation interferometer to give the two beams perpendicular polarization directions. Polymer polarizers could not be used because the high intensity of the beams would destroy them. To save space in the interferometer, the two IR mirrors are used as reflecting polarizers.

Reflecting polarizers exploit the fact that some materials reflect the s and p polarization at different rate. Putting a dielectric at the Brewster angle will make sure that the p polarization is not reflected at all, leading to only s polarization being further propagated [8].

As mentioned before, the total reflection angle of the two mirrors is 12°, or 6° per mirror. This corresponds to an incidence angle of 84°. This is far from the Brewster angle of any common optical materials, but some semiconductors have extreme refractive indices and thus very large Brewster angles.

Germanium has a refractive index of about 4.7 at 800 nm wavelength [29]. This means a Brewster angle of

$$\theta_{\mathrm{B}} = \tan^{-1}\left(\frac{n_2}{n_1}\right) = \tan^{-1}\left(\frac{4.7}{1}\right) = 77.99°. \tag{12}$$

Figure 27 shows the reflection as a function of incidence angle for the two polarizations.

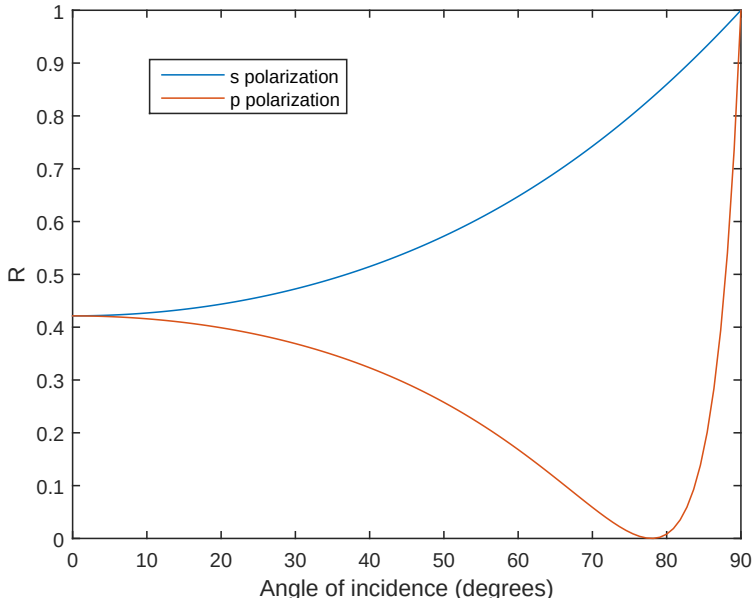

Figure 27: Reflection as a function of incidence angle for s and p polarization.

As can be seen in the plot, 84° is close enough to θ_{B} that at this angle, the mirrors have a reflectance of 91.5% for s polarization and 10.9% for p polarization. Thus, for each reflection on a germanium mirror, the s component is reflected more than 8 times more effectively than the p component.

For further discrimination, the second holey mirror can also be left uncoated. Being made out of fused silica, it will have a reflectivity of around 40% for the s polarization and 20% for p polarization [29].

Letting the alignment beam be s polarized, the original polarization of the laser beam, therefore leads to it being favored by a factor 140 over the pump IR.

However, the s polarization is also necessary for the XUV beam; if it is p polarized the reflectivity of the fused silica plate will drop by 20% [30]. Since the generated harmonics have the same polarization as the generating field, it is advantageous for the generating field to be vertically polarized (s) before generation. This means that the post-generation interferometer also needs a half-wave plate before the germanium plates mirrors.

In many pump-probe experiments it is necessary for the pump and probe to have the same polarization. In this case, one may use the half-wave plate in the post-generation interferometer to rotate the polarizations of the two beams slightly less than 90°. Leaving a few percent of s polarization to the pump IR will make sure it is predominantly s polarized, while keeping it weaker than the alignment pulse. Figure 28 shows the various polarizations in this scheme.

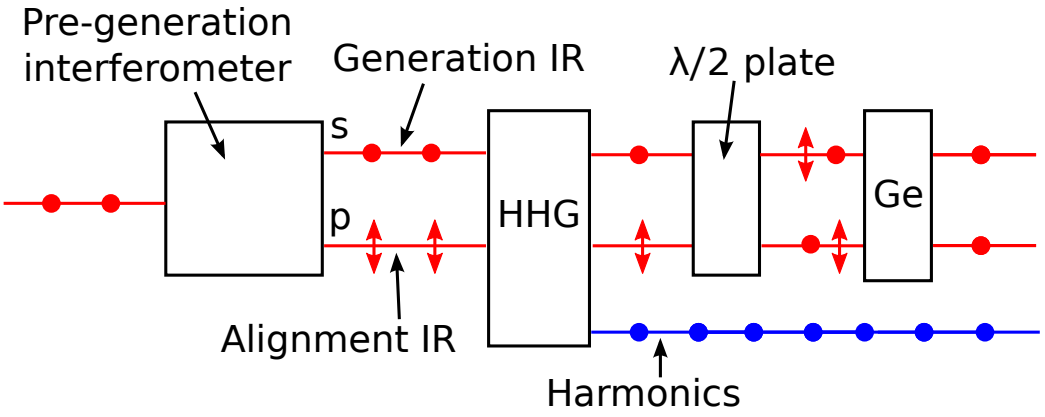

Figure 28: An example of a polarization scheme used in the post-generation interferometer.

3.6 Design and testing

Dassault Systèmes SolidWorks was used to plan the setup and design the holey mirrors as well as several support components. Figure 29 presents a rendering from SolidWorks, showing approximately how the setup would look outside the vacuum chamber.

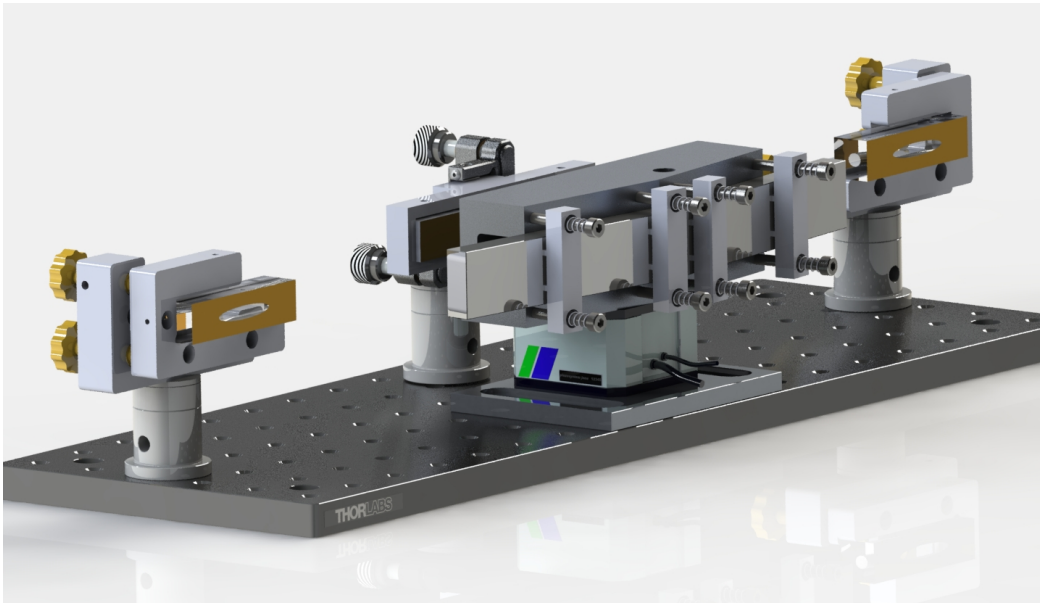

Figure 29: A computer generated image of the post-generation interferometer.

To test the design of the interferometer, Photon Engineering FRED was used.

For the purposes of this thesis work, its raytracing capabilities were used to estimate the stability range of the interferometer by checking the number of rays arriving at the focus at various positions of the translation stage.

The wave propagation tools were used in making estimates of the beam intensities at various points in the interferometer, in the course of design. Figure 30 on the following page is an example of this, and shows the intensity of the alignment beam at the second focus (molecular target).

Notably, a ring pattern can be seen, which is the result of the alignment beam getting an annular character in the holey mirrors of the post-generation interferometer.

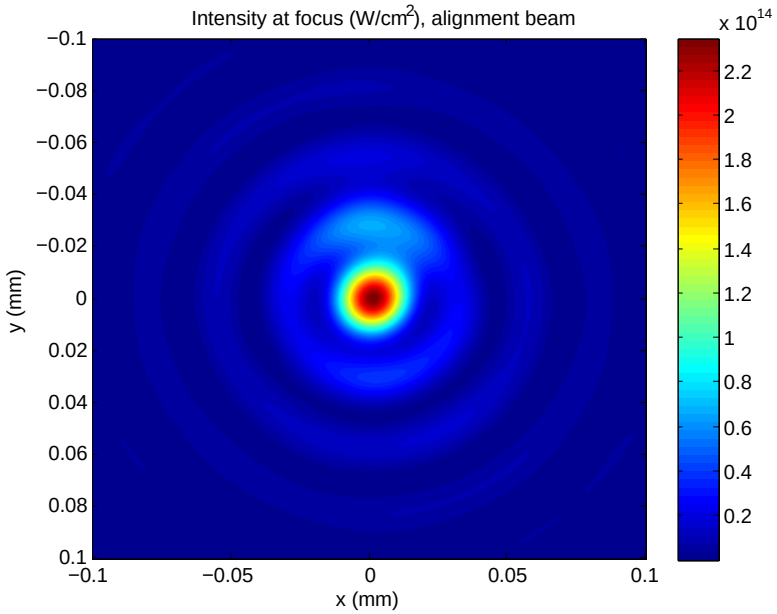

Figure 30: The intensity at target focus of the alignment beam.

3.7 Design challenges

The size of the XUV beam was measured in the current setup's diagnostics chamber. It was determined that the edges of the beam were 7 mm apart and, assuming that this corresponds to 1% intensity, the waist size[5] was 2.305 mm.

In order to get a strong XUV signal at the target, it is important not to clip it, therefore one would want a large opening in the holey mirrors of the post-generation interferometer.

However, this also means that the alignment beam must have a certain size in order not to be fully transmitted into the XUV arm of the post-generation interferometer, where it will be attenuated by the filters and anti-reflection coating. This in turn means a large hole size in the holey mirrors of the pre-generation interferometer, and thus less energy available for generation. Figure 31 on the next page shows the parameters discussed here.

To determine whether the placement of the post-generation interferometer has an influence on these conditions, the alignment beam and the XUV beam

[5]For Gaussian beams the waist size W is assumed to be half the width at which the beam has an intensity of $1/e^2$ times the maximum intensity.

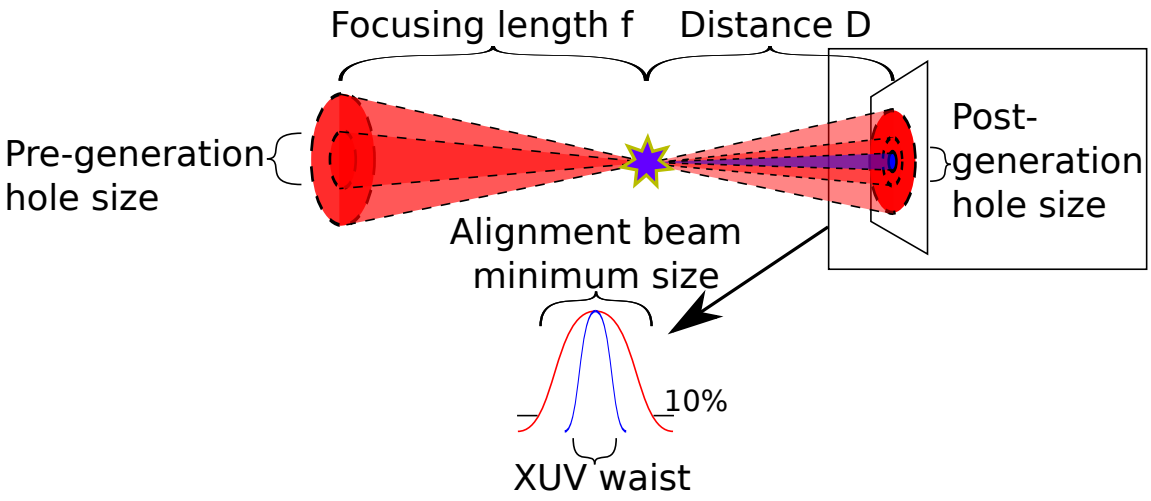

Figure 31: A sketch of the beam sizes and distances to take into account.

were propagated from the focus.

According to these calculations, the ratio W_A/W_{xuv} between the waist sizes of these two beams is approximately constant from a distance D of more than 1 m. Since it would be impossible to place the interferometer any closer than 1 m, the current placement of the diagnostics chamber ($D = 5$ m) was determined to be as good as any.

An iterative process was used to calculate the transmission parameters of the interferometer setup, using the following steps:

1. Set a hole size for the first holey mirror of the post-generation interferometer (a scan was perfomed from 1 to 10 mm).

2. Calculate the transmission of the XUV beam through this hole, using the relation [8]

$$P(\rho) = 1 - \exp\left(\frac{-2\rho^2}{2W^2}\right), \tag{13}$$

   where ρ is the hole size.

3. Calculate a waist size of the alignment beam for which no more than 90% is transmitted through the hole, i.e. at least 10% is reflected on the holey mirror[6]. This is easily done as the inverse of the equation

[6]To introduce similar losses in the probe IR beam one may use an iris-style aperture to clip its edges.

above.

4. When $W_A(D)$, the size of the alignment beam at D, is known, its size on the other side of the focus can be calculated as $W_A(D) \cdot \frac{f}{D}$.

   This is the size the hole of the pre-generation interferometer holey mirrors must have in order for the alignment beam to have the size calculated in the previous step.

5. Finally, using the calculated hole size, calculate the amount of IR power which is diverted from generation, again using Equation (13) on the preceding page.

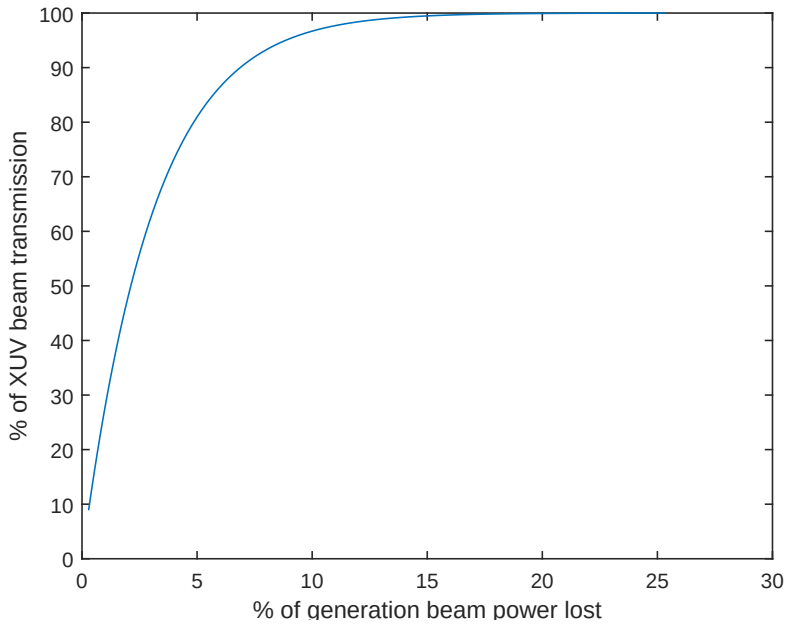

Figure 32: How much XUV is lost in the post-generation interferometer versus how much generation IR is lost in the pre-generation interferometer.

Figure 32 shows a plot of the XUV transmission from step 2 compared to the generation beam loss calculated in step 5. At this point it's possible to decide which transmission of the XUV is needed, and then whether or not the loss in generation IR is acceptable.

An XUV transmission of 95% was deemed acceptable. This corresponds to an post-generation interferometer hole size of 5.63 mm. The generation

beam loss at this point is 8.9%, or just over 5 mJ for a 60 mJ beam. Judging by the experiments performed, this loss is manageable.

4 Conclusion

The proposed setup fulfills all the desired specifications given in the introduction. For this setup design to be viable, it is necessary for HHG with annular beams to work well. Experiments and simulations show that this is indeed the case.

The setup will enable XUV-IR pump-probe experiment with a few-attosecond resolution, along with molecular alignment experiments, or a combination of these such as XUV ionization of aligned molecules, perturbed by a IR field.

4.1 Outlook

4.1.1 Construction of post-generation interferometer

Many parts of the post-generation interferometer are completely custom made. The holey mirrors are bored at a much smaller angle than normal holey mirrors. Germanium is commonly used for much longer IR wavelengths (where it is transparent), and thus normally not available with a surface finish suitable for 800 nm, which has made the polarizing mirrors difficult to purchase.

Because of this, at the time of writing, many parts have not arrived and thus it was not possible to construct the interferometer or do any testing. This is a task for the future.

4.1.2 Alternative design for pre-generation interferometer

One way of avoiding the problem of alignment pulse attenuation (mentioned in Section 3.7 on page 38) is to use beamsplitters (based on polarization-dependent multilayer coating) in the pre-generation interferometer. Initial simulations have shown that a 93-7 beamsplitter (giving the alignment beam 7% energy) could give the desired final ratio between the alignment and pump IR, without being dependent on a large hole in the splitting mirrors.

This would require some redesigns of the pre-generation interferometer, as larger mirrors and a larger wave plate would be needed in the alignment beam arm.

4.1.3 Split mirror

The XUV mirror in the post-generation interferometer design can be replaced with a split mirror. The split mirror consists of two glass plates controlled by translation stages, each of which reflects half of the XUV beam [31].

This design makes it possible to split the XUV pulse in two and delay the parts in respect to each other for autocorrelation experiments, for example.

In combination with the interferometers proposed in this thesis, this would also make it possible to perform XUV-XUV-IR pump-probe experiments, possibly in combination with molecular alignment. The sheer number of possible pulses and pump-probe schemes makes this a very attractive proposition for molecular physics.

5 Acknowledgements

Warm thanks go firstly to my supervisors Piotr Rudawski, Bastian Manschwetus and Per Johnsson for always being available to provide insight into the science of the work, or the workings of the lab at the high intensity harmonics beamline. I'm further indebted to Anne l'Huillier for giving me the opportunity to perform this work.

Others who helped out with the experiments performed at the high intensity beamline were Sylvain Maclot (who also provided a program to help present the results), Hélène Coudert-Alteirac and Linnea Rading. For the simulations I was dependent on the coding help of David Kroon.

Further, Christoph Heyl let me use some excellent graphics on the beamline, Marija Kotur explained RABITT, Chen Guo gave me an introduction to interferometer design, Stefanos Carlström provided input on analysis of results, Eleonora Lorek gave useful insight into growing semiconductors and Neven Ibrakovic showed me the basics of SolidWorks. Finally, I extend my thanks to everyone at the atomic physics division for providing a motivating and pleasant place to work.

References

[1] M. Baker, "Faster frames, clearer pictures," *Nature Methods*, vol. 8, no. 12, pp. 1005–1009, 2011.

[2] L. E. Hargrove, R. L. Fork, and M. A. Pollack, "Locking of He-Ne laser modes induced by synchronous intracavity modulation," *Applied Physics Letters*, vol. 4, no. 1964, pp. 12–14, 1964.

[3] R. L. Fork, C. H. Cruz, P. C. Becker, and C. V. Shank, "Compression of optical pulses to six femtoseconds by using cubic phase compensation.," *Optics letters*, vol. 12, no. 7, pp. 483–485, 1987.

[4] F. Krausz, M. E. Fermann, T. Brabec, P. F. Curley, M. Hofer, M. H. Ober, C. Spielmann, E. Wintner, and A. J. Schmidt, "Femtosecond Solid-State Lasers," *Journal of Quantum Electronics*, vol. 28, no. 10, 1992.

[5] B. Nordén, "Extended version of the press release for the Nobel Prize in Chemistry 1999," *The Royal Swedish Academy of Sciences*, vol. -, pp. –, 1999.

[6] P. B. Corkum and Z. Chang, "The Attosecond Revolution," *Optics and Photonics News*, vol. 19, no. 10, p. 24, 2008.

[7] P. H. Bucksbaum, "The Future of Attosecond Spectroscopy," *Science (New York, N.Y.)*, vol. 317, no. August, pp. 766–769, 2007.

[8] B. E. A. Saleh and M. C. Teich, *Fundamentals of Photonics*. Wiley, 2nd ed., 2007.

[9] M. Wulff, D. Khakhulin, Q. Kong, J. H. Lee, T. K. Kim, M. Cammarata, S. Bratos, J.-C. Leichnam, F. Schotte, and P. A. Anfinrud, "Molecular Dynamics Probed by Short X-ray Pulses from a Synchrotron," in *The Future of Dynamic Structural Science*, ch. 19, pp. 261–284, 2014.

[10] J. R. Schneider, R. Haugaard Nielsen, J. Feldhaus, B. Keitel, L. Wiebke, P. Schmüser, B. Sonntag, and K. Tiedtke, "FLASH: The Free-Electron Laser in Hamburg," p. 56, 2007.

[11] N. H. Burnett, H. A. Baldis, M. C. Richardson, G. D. Enright, N. H. Burnett, H. A. Baldis, M. C. Richardson, and G. D. Enright, "Harmonic generation in CO_2 laser target interaction," *Applied Physics Letters*, vol. 31, pp. 172–174, 1977.

[12] X. F. Li, A. L'Huillier, M. Ferray, L. A. Lompré, and G. Mainfray, "Multiple-harmonic generation in rare gases at high laser intensity," *Physical Review A*, vol. 39, no. 11, pp. 5751–5761, 1989.

[13] M. Lewenstein, P. Balcou, M. Y. Ivanov, and A. L'Huillier, "Theory of high-harmonic generation by low-frequency laser fields," *Physical Review A*, vol. 49, no. 3, 1994.

[14] P. Rudawski, C. M. Heyl, F. Brizuela, J. Schwenke, A. Persson, E. Mansten, R. Rakowski, L. Rading, F. Campi, B. Kim, P. Johnsson, and A. L'Huillier, "A high-flux high-order harmonic source," *Review of Scientific Instruments*, vol. 073103, no. May 2015, 2014.

[15] P. B. Corkum and F. Krausz, "Attosecond science," *Nature Physics*, vol. 3, pp. 381–387, 2007.

[16] H. G. Muller, "Reconstruction of attosecond harmonic beating by interference of two-photon transitions," *Applied Physics B (Supplement)*, vol. 74, pp. 17–21, 2002.

[17] P. M. Paul, E. S. Toma, P. Breger, G. Mullot, F. Auge, P. Balcou, H. G. Muller, and P. Agostini, "Observation of a train of attosecond pulses from high harmonic generation.," *Science (New York, N.Y.)*, vol. 292, pp. 1689–92, June 2001.

[18] F. Krausz and M. Ivanov, "Attosecond physics," *Reviews of Modern Physics*, vol. 81, no. 1, pp. 163–234, 2009.

[19] J. Itatani, G. L. Yudin, F. Krausz, and P. B. Corkum, "Attosecond Streak Camera," *Physical Review Letters*, vol. 88, no. 17, pp. 1–4, 2002.

[20] Z. Chang, *Fundamentals of Attosecond Optics*, vol. 2. CRC Press, 1st ed., 2011.

[21] "nanoX 400 data sheet," *Piezosystem Jena homepage*.

[22] H. Stapelfeldt and T. Seideman, "Colloquium : Aligning molecules with strong laser pulses," *Reviews of Modern Physics*, vol. 75, no. April, 2003.

[23] H. Wikmark, "High-order harmonic generation using variably polarized two-color fields," B.Sc. thesis, Lund University, 2013.

[24] P. Rudawski, *Second-generation High-Order Harmonic Sources From CPA to OPCPA*. PhD thesis, Lund University, Faculty of Engineering, 2014.

[25] C. Heyl, *Scaling and Gating Attosecond Pulse Generation*. PhD thesis, Lund University, Faculty of Engineering, 2014.

[26] J. Peatross, "High-order harmonic generation with an annular laser beam," vol. 19, no. 13, pp. 942–944, 1994.

[27] F. Frank, C. Arrell, T. Witting, W. a. Okell, J. McKenna, J. S. Robinson, C. a. Haworth, D. Austin, H. Teng, I. a. Walmsley, J. P. Marangos, and J. W. G. Tisch, "Invited review article: technology for attosecond science.," *The Review of scientific instruments*, vol. 83, p. 071101, July 2012.

[28] L. Roos, *Optimisation and Application of Intense High-Order Harmonic Pulses*. PhD thesis, Lund University, Faculty of Engineering, 2001.

[29] D. E. Aspnes and A. A. Studna, "Dielectric functions and optical parameters of Si, Ge, GaP, GaAs, GaSb, InP, InAs, and InSb from 1.5 to 6.0 eV," *Physical Review B*, vol. 27, no. 2, pp. 985–1009, 1983.

[30] B. Henke, E. Gullikson, and J. Davis, "X-Ray Interactions: Photoabsorption, Scattering, Transmission, and Reflection at E = 50-30,000 eV, Z = 1-92," *Atomic Data and Nuclear Data Tables*, vol. 54, no. 2, pp. 181–342, 1993.

[31] F. Campi, H. Coudert-Alteirac, M. Miranda, L. Rading, B. Manschwetus, P. Rudawski, A. L'Huillier, and P. Johnsson, "Design and test of a broadband split-and-delay unit for attosecond XUV-XUV pump-probe experiments," *Manuscript in Preparation*, 2015.